
CMS Physics Analysis Summary

Contact: cms-pag-conveners-b2g@cern.ch

2015/09/02

Search in two-dimensional mass space for
 $T'\bar{T}' \rightarrow W'^+bW'^-\bar{b}$ in the dilepton final state in
proton-proton collisions at $\sqrt{s} = 8$ TeV

The CMS Collaboration

Abstract

A search for $T'\bar{T}' \rightarrow W'^+bW'^-\bar{b}$ in the dilepton final state is presented using pp collision data recorded by the CMS detector corresponding to 19.7 fb^{-1} of integrated luminosity. The analysis is based on a two-dimensional mass reconstruction of the $T'\bar{T}'$ system performed without assumptions about the underlying theory except the event topology. No significant excess over the standard model predictions is observed. We set 95% confidence level upper limits on a simplified little Higgs model.

1 Introduction

After the discovery of a new particle with a mass of $125 \text{ GeV}/c^2$ consistent with the Higgs boson [1], the evidence for the existence of new physics at the TeV scale is even stronger: new particles are needed in order to keep the radiative corrections of the Higgs boson mass to the electroweak scale. The above is an indication of the so-called hierarchy problem, which is guiding the efforts of many Beyond Standard Model (BSM) theories. Some of them try to solve the problem by predicting a "mirror" world, responsible for cancellations in these corrections. Part of this world is often both a new heavy top partner and new heavy gauge bosons [2, 3].

In this analysis we search for anything decaying like top pairs ($T'\bar{T}' \rightarrow W'^+bW'^-\bar{b}$), in their dilepton final state in which both W' bosons decay leptonically. So we are searching simultaneously for both a new heavy top partner and a new heavy charged gauge boson. We use pp collision data recorded by the CMS detector during 2012 and corresponding to 19.7 fb^{-1} of integrated luminosity. The final state has two charged leptons, two jets and missing transverse energy due to the invisible neutrinos. The analysis is based on a two-dimensional mass reconstruction of the $T'\bar{T}'$ system as described in [4]. The analytic solutions together with constraints from the parton distribution functions (PDFs) are used to reconstruct the masses of two unknown particles simultaneously. The only assumption used in the mass reconstruction is that each T' decays to a W' and a b quark, with the heavy W' subsequently decaying into an electron or a muon, and a massless particle. Thus, the analysis is performed in a model independent way to target possible signals that may have not been predicted yet. A hypothetical signal, based on the littlest Higgs model [5, 6] is used to set 95% CL upper limits on the production cross section times branching ratio as a function of the T' and the W' mass. Little Higgs models introduce spontaneously broken global symmetries due to a mechanism called "collective symmetry breaking" where the Higgs field appear as a pseudo-Nambu-Goldstone boson. The quadratic divergences are cancelled due to new heavy gauge bosons and quarks.

There are two major issues in searches for BSM models with missing energy: the difficulty in establishing a discovery and the even harder task of understanding the specific BSM model found (e.g the masses and spin of the new particles). The first difficulty is due to the fact that the experimental BSM searches are often based on missing energy related observables where the new physics appears in the tail of the distribution. This is different than the discovery of the Higgs boson where the mass peaks have large shape difference when compared with the background. After a possible observation of an excess of events in the tail of a distribution, our knowledge about the new theory will still be limited: the particle content, the masses and the spin of new particles will be unknown.

The search in two-dimensional mass space performed in this analysis targets both the above problems. The reconstruction of mass peaks of the two unknown particles concentrates signal events in a small region of the two-dimensional mass space whereas background events have no reason to do the same. The reconstructed masses also give valuable information about the particle content and thus the parameters of the model. The search in two-dimensional mass space can be extended to similar symmetric topologies predicted by other BSM theories with final states with two invisible particles.

This paper is organized as follows: the CMS detector is presented in section 2. The samples used and the event selection are described in sections 3 and 4. The two-dimensional mass reconstruction is presented in section 5. Finally, the systematic uncertainties and the limits are presented in sections 6 and 7 respectively.

2 CMS Detector

The central feature of the Compact Muon Solenoid (CMS) apparatus is a superconducting solenoid of 6 m internal diameter, providing a magnetic field of 3.8 T. The superconducting solenoid volume contains a silicon pixel and strip tracker, a lead tungstate crystal electromagnetic calorimeter (ECAL), and a brass and scintillator hadron calorimeter (HCAL), each composed of a barrel and two endcap sections. Muons are measured in gas-ionization detectors embedded in the steel flux-return yoke outside the solenoid. The silicon tracker measures charged particles within the pseudorapidity η range $|\eta| < 2.5$. For not-isolated particles with transverse momenta of $1 < p_T < 10$ GeV and $|\eta| < 1.4$, the track resolutions are typically 1.5% in p_T , and, respectively, between 25-90 and 45-150 μm in transverse and longitudinal impact parameters relative to the production vertex [7]. The electromagnetic calorimeter is made of lead tungstate crystals, and provides a coverage of $|\eta| < 1.479$ in the barrel region, and $1.479 < |\eta| < 3.0$ in the endcaps. The ECAL energy resolution for electrons from $Z \rightarrow e^+e^-$ decays is smaller than 2% in the central region of the ECAL barrel ($|\eta| < 0.8$), and is between 2% and 5% elsewhere [8]. The HCAL consists of a sampling calorimeter that has alternating layers of brass as absorber and plastic scintillator as active material, covering the pseudorapidity range $|\eta| < 3$, which is extended to $|\eta| < 5$ through forward calorimetry. Muons are measured in the pseudorapidity range $|\eta| < 2.4$, with detection planes made using three technologies: drift tubes, cathode-strip chambers, and resistive-plate chambers. Matching muons to tracks measured in the silicon tracker, results in a relative resolution in p_T for muons with $20 < p_T < 100$ GeV of 1.3 – 2.0% in the barrel and less than 6% in the endcaps.

A more detailed description of the CMS detector, together with a definition of the coordinate system and kinematic variables, can be found in Ref. [9].

3 Simulated samples

The generation of the signal samples is performed using the littlest Higgs model. For the production, the Whizard 2.2.0 event generator [10, 11] is used in a grid of the two-dimensional mass plane of T' and W' . The range for both masses is up to 2 TeV using steps of 200 GeV. Only points in the grid where the mass of the heavy top partner is larger than that of the heavy gauge boson are produced. The free parameters of the model are highly restricted by the masses $M_{T'}$ and $M_{W'}$. Initially, the hard scattering ($pp \rightarrow T'\bar{T}'$) is generated with Whizard. The decays of both T' and W' is performed using Pythia 6.424 [12] and a flat matrix element in order to create a simplified model which is associated to models with similar particle content and masses. Samples produced with Whizard use the CTEQ6L PDF parametrization [13].

Top-pairs and single top samples are generated with Powheg 1.0 [14–16] combined with Pythia 6.424. The top pair sample is produced using the CT10 PDF set and the single top samples using the CTEQ6M PDF parametrization. Single boson samples (Drell-Yan, W +jets), are produced with Madgraph 5.1.1 [17] and are matched to Pythia 6.424 for parton showering. The same generator is used for the associated production of top pairs with a W/Z boson ($t\bar{t} + W/Z$). Samples produced with Madgraph use the CTEQ6L PDF parametrization. During the parton matching using Pythia, the MLM algorithm [18] is applied to avoid double counting of partons. Finally, diboson (WW , WZ , ZZ), QCD multi-jet and $t\bar{t} + \text{Higgs}$ samples are produced using Pythia 6.424. The underlying event is characterized using the Pythia Z2 tune [19].

Additional pp interactions in the same bunch crossing (pileup) are modelled by superimposing simulated minimum-bias events to the generated hard interactions. The simulated events are reweighted to reproduce the pileup multiplicity observed in data. Corrections are also applied

to the simulated events to take into account the differences between data and simulation for the trigger efficiencies, lepton identification, jet energy scale and resolution [8, 20–23].

4 Event Reconstruction and Selection

The search for new physics presented in this article utilizes the data collected in 2012, at a center of mass energy of $\sqrt{s} = 8$ TeV. The data recorded during this year correspond to an integrated luminosity of 19.7 fb^{-1} . For this analysis, the single muon and double electron triggers are used. The single muon trigger requires an isolated muon with transverse momentum of at least 40 GeV. The double electron trigger requires two isolated electrons with transverse momentum at least 17 and 8 GeV for the most energetic and the second most energetic electron respectively. The impact of pileup is minimized by requiring all charged particles to originate from the primary vertex.

Reconstruction of physics objects in both data and simulated samples is performed using the particle-flow algorithm [24]. Each single particle is reconstructed and identified with an optimized combination of all subdetector information. The energy of photons is directly obtained from the ECAL measurement, corrected for zero-suppression effects. The energy of electrons is determined from a combination of the electron momentum at the primary interaction vertex as determined by the tracker, the energy of the corresponding ECAL cluster, and the energy sum of all bremsstrahlung photons spatially compatible with originating from the electron track. The energy of muons is obtained from the curvature of the corresponding track. The energy of charged hadrons is determined from a combination of their momentum measured in the tracker and the matching ECAL and HCAL energy deposits, corrected for zero-suppression effects and for the response function of the calorimeters to hadronic showers. Finally, the energy of neutral hadrons is obtained from the corresponding corrected ECAL and HCAL energy.

Muons need to have a reconstructed track in both the tracker and in the muon system [21, 22]. The two tracks are then matched with a global fit requiring a small normalized χ^2 in order to suppress hadronic punch-through and muons from decays in flight. Reduction of the fraction of fake muons is performed with additional cuts such as the number of muon and tracker hits. Cosmic ray muons are reduced with cuts around the primary vertex in the xy and z plane. The muon transverse momentum has to be larger than 50 GeV and the muon pseudorapidity is restricted to 2.1 due to the single muon trigger acceptance. Additionally muons are required to be isolated in a cone of $\Delta R = \sqrt{\eta^2 + \phi^2} < 0.4$. The isolation observable is based on particle flow particles in this cone and has to be less than 20% of the muon transverse momentum.

Electrons are reconstructed as clusters in the electromagnetic calorimeter which are consistent with a track in the silicon tracker [8, 20]. Identification criteria include the distances in pseudorapidity and azimuthal angle between the cluster and the track, as well as shower shape variables. The momentum measured in the tracker has to be close to the energy deposit in the electromagnetic calorimeter. In addition, the ratio of the energy deposited in the hadronic and the electromagnetic calorimeter has to be small for electrons and photons. The electron track has to be close to the primary vertex in the xy and z plane. Electrons are required to have a transverse momentum greater than 50 GeV and to be in the acceptance of the electromagnetic calorimeter. The isolation observable for the electrons is based on the sum of transverse momenta of the particle flow objects in a cone of $\Delta R = 0.3$ and has to be smaller than 15% of the electron transverse momenta.

The reconstructed particles (except isolated leptons) are clustered into jets using the anti-kT algorithm [25] with a cone of $\Delta R = 0.5$. Jets are required to have a transverse momentum

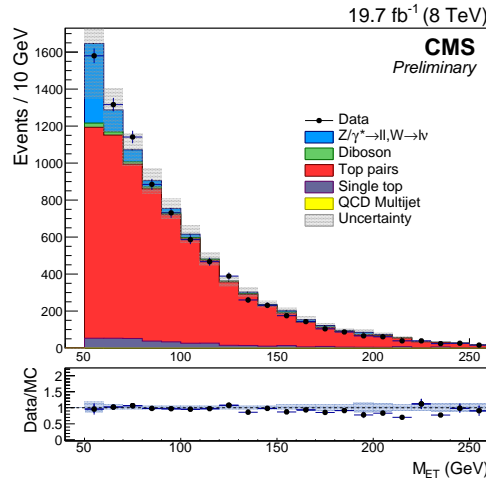


Figure 1: The missing energy distribution after all selection requirements. The hatched bands represent all the statistical and systematic uncertainties on the predicted background.

greater than 50 GeV and to be in the pseudorapidity region of $|\eta| < 2.4$. Corrections are applied to the simulated events for both the scale and the resolution of jets [23]. The missing energy is defined as the magnitude of the negative vector sum of all reconstructed particles. Events in this analysis are required to have more than 50 GeV of transverse missing energy.

We are searching for topologies similar to top pairs in the dilepton decay mode. The experimental signature consists of 2 leptons, 2 jets and missing energy in the event. Leptons are sorted by their transverse momentum p_T and the two most energetic leptons which satisfy the lepton identification criteria are selected. The two leptons are additionally required to be isolated, have high transverse momenta and invariant mass off-peak with respect to the Z boson resonance. Events are categorized into those containing 2 muons ($\mu\mu$), 2 electrons (ee), or 1 electron and 1 muon ($e\mu$). The jets are also sorted by their p_T , and the two most energetic ones are chosen. Mass reconstruction requires the jets coming from the hard process, so no b-tagging is applied in order to keep the ordering in the transverse momentum. An alternative ordering based on the value of the btagging discriminator has also been checked. The p_T ordering is better except in the diagonal of the 2-dimensional mass plane where the energy of the jets is small. Finally, as signal includes two invisible particles, events are required to have large transverse missing energy. As described above, all leptons, jet p_T as well as MET cuts are set to the same value. No optimization is performed for the selection based on specific models. The missing energy after all selection requirements applied can be seen in Figure 1.

5 Two-dimensional Mass reconstruction

The dilepton $T'\bar{T}'$ pair system satisfies the energy momentum constraints in the T' quark and the W' boson decays for both branches of the symmetric topology. In addition, the missing energy originating from the two invisible neutrinos gives two additional constraints. This system of equations has an equal number of unknowns, that is the momenta of the two neutrinos. The system can be solved analytically provided that the masses of the particles are known [26, 27]. The input for the algorithm consists of the momentum of the visible particles (2 leptons and 2 jets), the two components of the transverse momentum (MET_x, MET_y) as well as the masses of T', W' particles. Each possible input can give zero, two or four different solutions. There are two possible combinations of jets and leptons originating from the same T' quark, giving in total up to eight solutions per event.

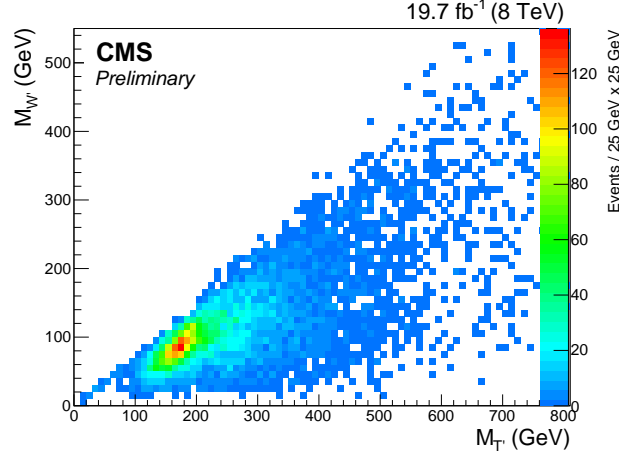


Figure 2: Mass reconstruction in two-dimensional mass space with the 2012 dataset (19.7 fb^{-1}).

Assuming the masses of the particles are unknown the only option is to test every point of the $M_{T'}$, $M_{W'}$ plane for possible solutions. The mass plane can be scanned in steps of 5 GeV to produce the area in which a specific solution exists or not. The solution area has mass information as it is bounded from below: there must be enough energy to produce the transverse components of the particles momenta. There is also an upper limit to the allowed masses produced due to the finite collision energy. Each parton takes only a fraction of the finite beam energy as described by its Parton Distribution Function (PDF). A single point in the solution area is chosen by picking the one which is more likely to originate from a proton-proton collision according to its PDF.

More specifically, each solution in a given mass point allows full reconstruction of the event kinematics from the neutrino momenta up to the $T'\bar{T}'$ four-vector. Knowledge of the $T'\bar{T}'$ system allows the calculation of the fraction of the beam energy of the two partons participating in the hard scattering ($x_{1,2} = (E_{(T'\bar{T}')} \pm P_{z(T'\bar{T}')}) / (2\sqrt{s})$). For each parton with fraction x_i a probability $F(x_i, Q)$ is estimated for the parton to originate from a proton. A weight per mass point is estimated by summing all possible parton combinations ($gg, u\bar{u}, \bar{u}u, d\bar{d}, \bar{d}d$). The weight can be written as:

$$\sum_{a,b} F_a(x_1, Q) F_b(x_2, Q), \quad (1)$$

where the summation in the pairs (a,b) is over the combinations mentioned above and F is the CT10 PDF-set [28] with momentum transfer $Q^2 = m_{T'}^2$. In order to restore solutions lost due to mismeasured particles each event is smeared to create N test events according to detector resolution. The leptons are smeared by 1% and the jets according to the Jet Energy Scale (JES) uncertainties [23]. Then the PDF weight distribution described above is averaged over all test events and normalized to unit volume to create a probability per mass point and solution:

$$P(M_{T'}, M_{W'}) = \frac{1}{V} \cdot \frac{1}{N} \sum_{i=1}^N \sum_{a,b} F_a^{(i)}(x_1, Q) \cdot F_b^{(i)}(x_2, Q) \cdot S^{(i)}(M_{T'}, M_{W'}) \quad (2)$$

where the summation is over the $N=100$ test events and flavour, V is the volume of the distribution and $S^{(i)}(M_{T'}, M_{W'})$ is the existence (or not) of a solution in a specific mass point. The maximum among all distributions related to different solutions gives the final $M_{T'}$ and $M_{W'}$.

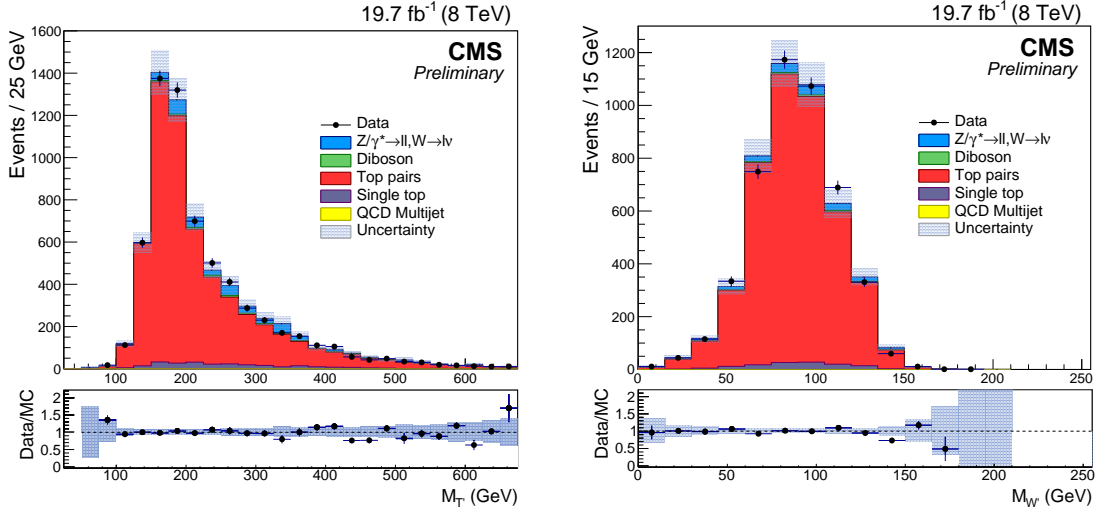


Figure 3: Top quark (left) and W boson mass (right) using the two-dimensional mass reconstruction. The hatched bands represent all the statistical and systematic uncertainties on the predicted background.

estimation per event. By applying the method in data corresponding to the 2012 dataset, the two-dimensional mass distribution can be created (Figure 2). Both top quark and W boson can be observed without any a priori knowledge of their masses or the underlying theory, except the event topology. Only data is used to construct Figure 2, no simulation is necessary for this observation. The top quark mass can be derived from the two-dimensional mass reconstruction using a range of 60-100 GeV for the W mass (Figure 3, left). In a similar way, the W boson mass is observed when using a range of 150-200 GeV for the top mass in Figure 3 (right). The performance of $M_{T'}$ and $M_{W'}$ reconstruction can be seen in Figure 4 for two different signal samples. Finally, the reconstructed $M_{T'}$ and $M_{W'}$ on top of its background are presented in Figure 5 and can be compared with the data distribution.

The event yields after mass reconstruction for both data and simulated background samples are presented in Table 1. The main background left are top-pairs (more than 85% of the total). Due to the good separation of signal and top pair background in the two-dimensional mass plane (Figure 5, left), the top pair region is an effective validation region for this background. More specifically, the top pair validation region is defined as the region $M_{T'} < 300$ GeV and $M_{W'} < 100$ GeV. This part of the mass plane is dominated by top pairs, with good agreement between data and simulation. If additionally the invariant mass of the $t\bar{t}$ system is smaller than 600 GeV, less than 1% of the signal events contaminate the validation region for any of the generated samples. The scale factor derived from the ratio of data over simulation is comparable to the top pair background systematic uncertainty and therefore no correction is applied in the signal region. The $M_{T'}$ and $M_{T'\bar{T}'}$ in the validation region can be seen in Figure 6 (left) and Figure 6 (right) respectively. The invariant mass of the $T'\bar{T}'$ system is an interesting observable to monitor for possible new heavy neutral gauge bosons ($Z' \rightarrow T'\bar{T}'$, $Z' \rightarrow t\bar{t}$). Finally, the Drell-Yan background is also evaluated in the Z-peak region where it is dominant by comparing data/simulation and a scale factor is derived in order to be used in the off-peak region.

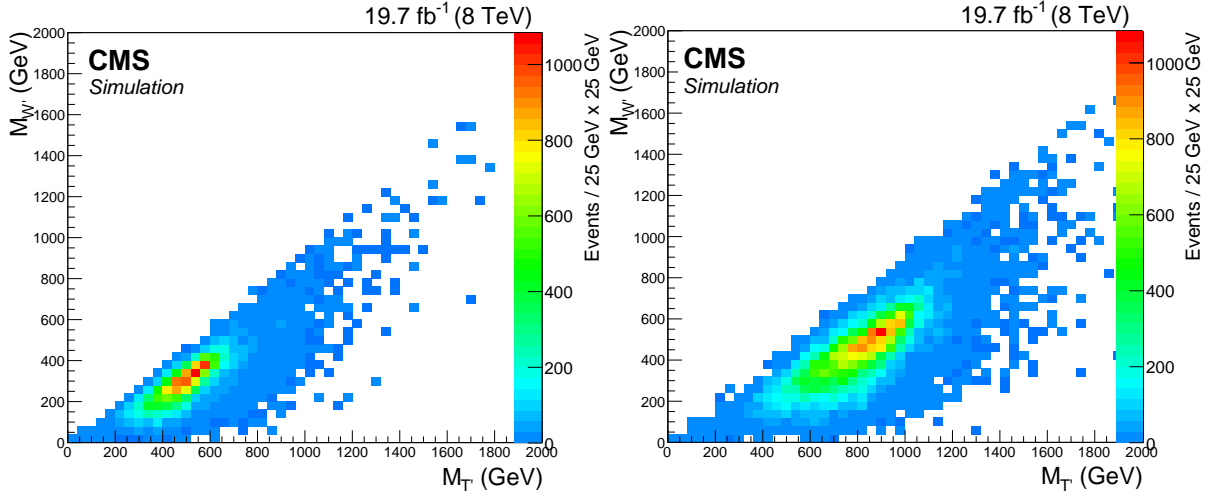


Figure 4: Two-dimensional mass reconstruction for $[M_{T'}, M_{W'}]=[600 \text{ GeV}, 400 \text{ GeV}]$ (left) and $[1000 \text{ GeV}, 600 \text{ GeV}]$ (right).

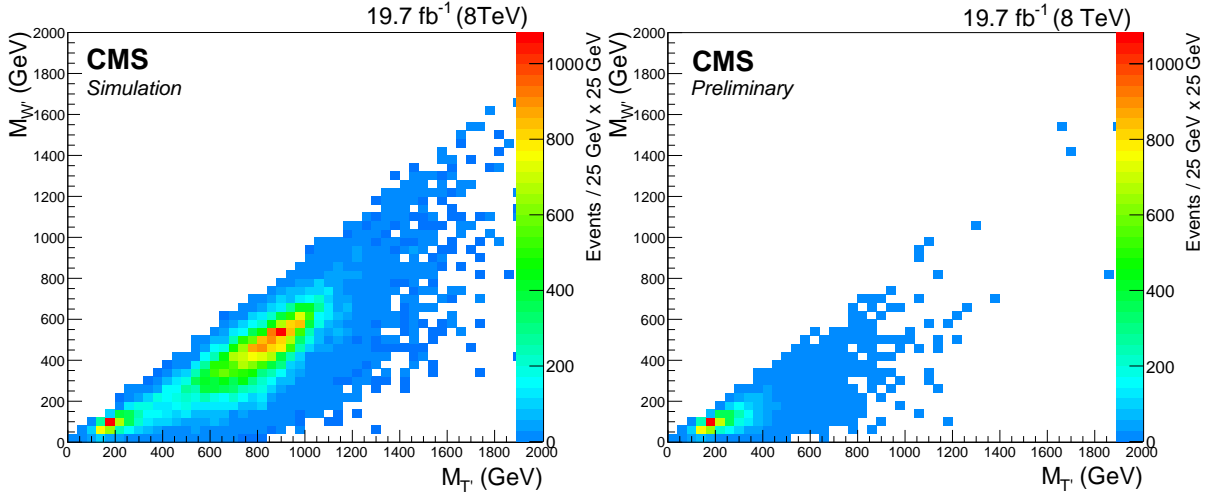


Figure 5: Two-dimensional mass reconstruction for signal and background for $M_{T'}=1000 \text{ GeV}$ $M_{W'}=600 \text{ GeV}$ (left), as well as, two-dimensional mass reconstruction for the 2012 CMS dataset (19.7 fb^{-1}) (right).

Sample	ee	$\mu\mu$	$e\mu$	total
TT+X	$1826.7 \pm 20.1 \pm 128.1$	$2077.3 \pm 21.5 \pm 145.7$	$3484.0 \pm 27.8 \pm 244.4$	$7387.9 \pm 40.5 \pm 518.3$
SingleTop	$89.2 \pm 6.3 \pm 44.7$	$113.4 \pm 7.1 \pm 56.8$	$188.8 \pm 9.1 \pm 94.7$	$391.3 \pm 13.1 \pm 196.2$
Z+Jets	$284.4 \pm 33.0 \pm 186.8$	$381.4 \pm 38.2 \pm 250.5$	$94.5 \pm 18.8 \pm 62.1$	$760.3 \pm 53.9 \pm 499.3$
Diboson	$34.4 \pm 1.7 \pm 10.4$	$36.0 \pm 1.7 \pm 10.9$	$51.8 \pm 2.2 \pm 15.7$	$122.2 \pm 3.3 \pm 37.1$
$T'_{800 \text{ GeV}} W'_{400 \text{ GeV}}$	$23.3 \pm 0.3 \pm 0.7$	$32.0 \pm 0.4 \pm 1.0$	$56.1 \pm 0.5 \pm 1.7$	$111.4 \pm 0.7 \pm 3.5$
$T'_{1000 \text{ GeV}} W'_{600 \text{ GeV}}$	$3.3 \pm 0.1 \pm 0.1$	$4.9 \pm 0.1 \pm 0.2$	$8.3 \pm 0.1 \pm 0.3$	$16.5 \pm 0.1 \pm 0.5$
Total Bkg	$2234.7 \pm 39.2 \pm 231.1$	$2608.1 \pm 44.4 \pm 295.5$	$3819.0 \pm 34.9 \pm 269.8$	$8661.8 \pm 68.7 \pm 746.9$
Obs. Ev.	2342	2358	3757	8457

Table 1: Background event yields for ee , $\mu\mu$, $e\mu$ and the combined dilepton channels in the two-dimensional search. The uncertainties on event yields include both statistical (first) and systematic (second) components.

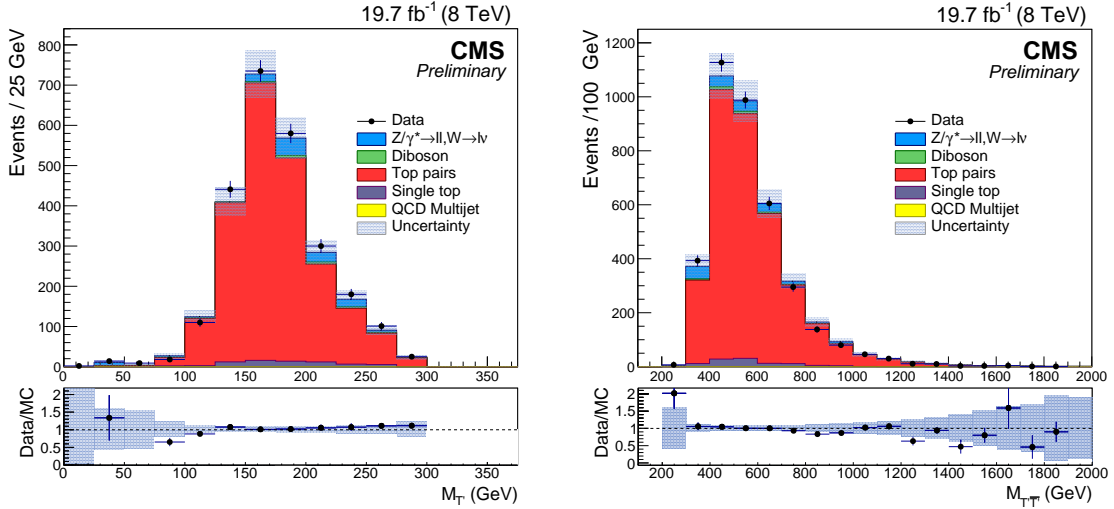


Figure 6: The invariant masses $M_{T\bar{T}}$ (left) and $M_{T\bar{T}\bar{T}}$ (right) in the top pairs validation region. The hatched bands represent all the statistical and systematic uncertainties on the predicted background.

6 Systematic Uncertainties

The rate and shape systematic effects for both signal and background processes are examined in this analysis. A list of corrections described in previous sections are applied in order to compensate for simulation mismodeling of efficiencies, energy scales and detector resolution. The variation of these scale factors by their uncertainties give an estimate on the related systematic effect.

More specifically, the uncertainty introduced by the modeling of pile-up events is estimated by shifting the minimum bias cross section by one standard deviation and recalculating the event weights for the simulated events. As already mentioned, corrections are applied to the trigger and reconstruction efficiencies to match those measured using data. These corrections are varied by their uncertainties in order to estimate the trigger and reconstruction efficiencies systematics for both electrons and muons [8, 20–22]. The jet energy scale systematic uncertainty is estimated by shifting the energy of the jets by one standard deviation as described in [23]. The jet energy resolution in simulation is also corrected to match the resolution observed in data: additional smearing is performed according to the data/simulation resolution ratio. The latter is varied by its uncertainty in order to estimate the jet energy resolution systematic effect.

The top pair samples are produced using tree-level processes (Madgraph + Pythia). The choice of renormalization and factorization scales introduces a systematic error which is estimated by variation of the scales in the generation process by a factor of 2. The calculation is performed using dedicated top pair simulation samples. The tree-level events produced by Madgraph are matched to the Pythia parton shower to model additional soft and co-linear radiation. The thresholds that control the matching of partons from the matrix element with those from parton showers are varied in order to estimate the relative change in the Monte-Carlo event yields. The diboson and single top samples normalization uncertainties are taken conservatively to be 30% and 50% respectively. For Drell-Yan, the percentage difference between Data/MC in the near Z peak region is used as a systematic uncertainty for this background [29]. The PDF uncertainty introduced to the reconstructed masses is estimated using the CT10 PDF error set [30]. The PDF parameters are changed within their uncertainties and the effect on the invariant mass

distributions is evaluated. There is no significant effect on either shape nor rate when using the above method or when using different PDF sets. A rate systematic uncertainty due to PDFs is assigned to top-pairs as described in [31]. The search is performed in a region where top-pairs are the dominant background, as can be seen in Table 1. The theoretical uncertainties related to their production have the largest impact on the total uncertainty of the estimated event yields. Finally, the uncertainty on the integrated luminosity is estimated to be 2.6% by an independent measurement [32]. A summary of all the systematic uncertainties considered can be seen in Table 2. As there are no significant shape effects only rates were considered in the estimation of the limits.

7 Limits

No evidence of any excess is found so an upper limit on the signal production cross-section per mass point is set. The signal limits are evaluated using a modified frequentist approach, the CL_s method [33]. The following background categories are used: $t\bar{t}$, single top, single boson (Drell-Yan) and dibosons. The low occupancy and possible bins with zero entries in the simulated 2-D distributions can affect the limit calculation. Therefore, the empty bins are merged with adjacent bins following a topological merging algorithm where bins with low occupancy are merged with their neighbors to form superbins. The merging scheme is derived using as input the histogram of the total background. The scheme is then used to merge in a similar way all the rest of the 2-D histograms used in the limit calculation. More specifically, for each bin in the 2-D histogram a superbin is created. The list of superbins is then searched for an empty superbin. If found, it is merged with the adjacent superbin with the smaller number of events. The algorithm is applied iteratively until no empty superbin is found.

The observed and expected limits are then calculated for all signal points created. The search region is defined by the grid of samples generated (lowest at $M_{T'} = 400$ GeV, $M_{W'} = 200$ GeV). Interpolation is used to estimate the limit for all other points internal in the region defined by the grid. The observed upper limit on the cross-section per $M_{T'}$ and $M_{W'}$ for this search region is presented in Figure 7. The limits for the different event categories are presented in Figure 8. For the simplified model based on littlest Higgs, the exclusion is up to a $M_{T'}$ range of 800-920 GeV, depending on $M_{W'}$.

Table 2: Summary for all systematic uncertainties. The theoretical uncertainties for top pair background are shown separately.

Source	T' 800 GeV W' 400 GeV	$t\bar{t} + X$	Dibosons (WW, WZ, ZZ)	Single Top	Z+jets
Luminosity	2.6%	2.6%	2.6%	2.6%	2.6%
PileUp modelling	0.4%	0.4%	3.0%	0.7%	4.7%
Trigger efficiency	1.0%	1.0%	1.0%	1.0%	1.0%
Muon id and isolation	1.2%	0.7%	0.8%	0.7%	0.8%
Electron id and isolation	0.5%	0.5%	0.5%	0.5%	0.5%
Jet energy scale	0.2%	1.1%	1.3%	1.3%	5.4%
Jet energy resolution	0.1%	0.7%	0.8%	1.6%	5.3%
Q^2 scale	-	5.3%	-	-	-
Matrix element/Parton shower	-	2.0%	-	-	-
Parton distribution functions	-	2.6%	-	-	-
Cross section	-	-	30%	50%	65%

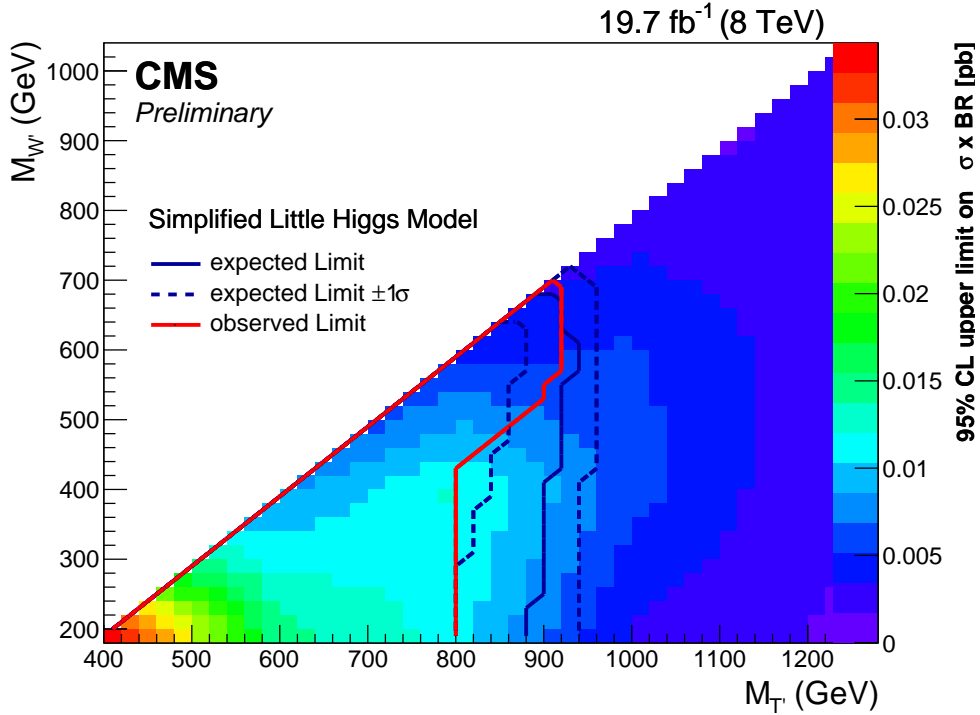


Figure 7: The expected and observed 95% CL upper limits on the $\sigma \times \text{BR}$ for the simplified Little Higgs Model.

8 Summary

A search for $pp \rightarrow T'\bar{T}' \rightarrow W'^+bW'^-\bar{b}$ in the dilepton final state has been performed using 19.7 fb^{-1} of data recorded by the CMS detector at $\sqrt{s} = 8 \text{ TeV}$. The analysis is based on a two-dimensional mass reconstruction of the $T'\bar{T}'$ system without assumptions about the underlying theory except the event topology. No deviation from standard model predictions is observed. The region excluded from the search region defined above is up to a $M_{T'}$ range of 800-920 GeV, depending on $M_{W'}$. This is the first dedicated search performed at the LHC for both a new heavy top partner and a new heavy charged gauge boson as predicted by the littlest Higgs model.

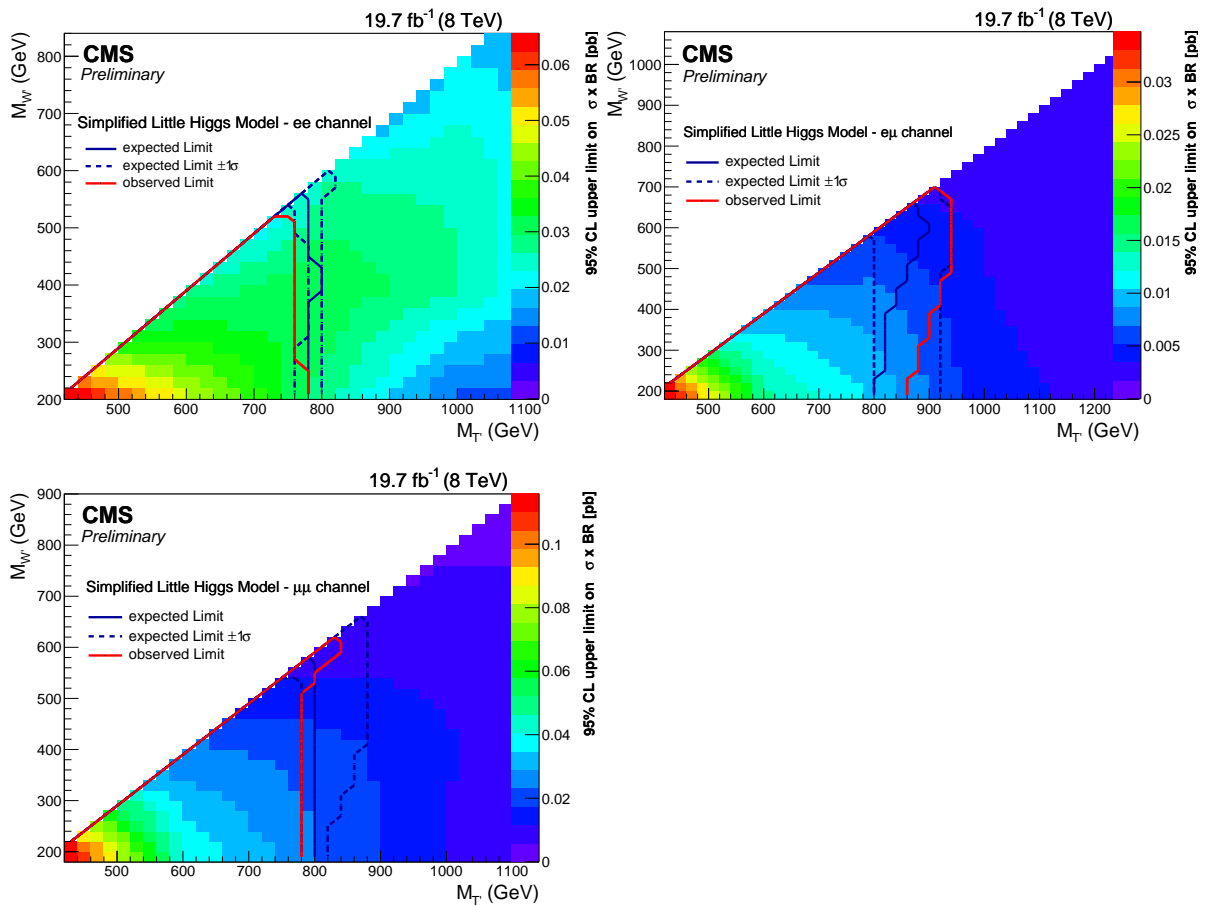


Figure 8: The expected and observed 95% CL upper limits on the $\sigma \times \text{BR}$ for electron-electron (top left), electron-muon (top right) and muon-muon (bottom left) event categories for the simplified Little Higgs Model.

References

- [1] CMS Collaboration, "Observation of a new boson at a mass of 125 GeV with the CMS experiment at the LHC", *Phys. Lett. B* **716** (2012) 30, doi:10.1016/j.physletb.2012.08.021, arXiv:1207.7235.
- [2] S. P. Martin, "A Supersymmetry primer", *Adv. Ser. Direct. High Energy Phys.* **18** (1997) 1, doi:10.1142/9789812839657_0001, 10.1142/9789814307505_0001, arXiv:hep-ph/9709356.
- [3] M. Schmaltz and D. Tucker-Smith, "Little Higgs review", *Ann. Rev. Nucl. Part. Sci.* **55** (2005) 229, doi:10.1146/annurev.nucl.55.090704.151502, arXiv:hep-ph/0502182.
- [4] G. Anagnostou, "Model Independent Search in 2-Dimensional Mass Space", in *2nd International Conference on New Frontiers in Physics*. EPJ Web of Conferences, Volume 71, 2014. doi:10.1051/epjconf/20147100006.
- [5] T. Han, H. E. Logan, B. McElrath, and L.-T. Wang, "Phenomenology of the little Higgs model", *Phys. Rev. D* **67** (2003) 095004, doi:10.1103/PhysRevD.67.095004, arXiv:hep-ph/0301040.
- [6] J. Reuter, M. Tonini, and M. de Vries, "Little Higgs Model Limits from LHC - Input for Snowmass 2013", arXiv:1307.5010.
- [7] CMS Collaboration, "Description and performance of track and primary-vertex reconstruction with the CMS tracker", *JINST* **9** (2014) P10009, doi:10.1088/1748-0221/9/10/P10009, arXiv:1405.6569.
- [8] CMS Collaboration, "Performance of electron reconstruction and selection with the CMS detector in proton-proton collisions at $\sqrt{s} = 8$ TeV", *JINST* **10** (2015) P06005, doi:10.1088/1748-0221/10/06/P06005, arXiv:1502.02701.
- [9] CMS Collaboration, "The CMS experiment at the CERN LHC", *JINST* **3** (2008) S08004, doi:10.1088/1748-0221/3/08/S08004.
- [10] W. Kilian, T. Ohl, and J. Reuter, "WHIZARD: Simulating Multi-Particle Processes at LHC and ILC", *Eur. Phys. J. C* **71** (2011) 1742, doi:10.1140/epjc/s10052-011-1742-y, arXiv:0708.4233.
- [11] M. Moretti, T. Ohl, and J. Reuter, "O'Mega: An Optimizing matrix element generator", arXiv:hep-ph/0102195.
- [12] T. Sjöstrand, S. Mrenna, and P. Skands, "PYTHIA 6.4 physics and manual", *JHEP* **05** (2006) 026, doi:10.1088/1126-6708/2006/05/026, arXiv:hep-ph/0603175.
- [13] P. M. Nadolsky et al., "Implications of CTEQ global analysis for collider observables", *Phys. Rev. D* **78** (2008) 013004, doi:10.1103/PhysRevD.78.013004, arXiv:0802.0007.
- [14] P. Nason, "A new method for combining NLO QCD with shower Monte Carlo algorithms", *JHEP* **11** (2004) 040, doi:10.1088/1126-6708/2004/11/040, arXiv:hep-ph/0409146.

- [15] S. Frixione, P. Nason, and C. Oleari, “Matching NLO QCD computations with parton shower simulations: the POWHEG method”, *JHEP* **11** (2007) 070, doi:10.1088/1126-6708/2007/11/070, arXiv:0709.2092.
- [16] S. Alioli, P. Nason, C. Oleari, and E. Re, “A general framework for implementing NLO calculations in shower Monte Carlo programs: the POWHEG BOX”, *JHEP* **06** (2010) 043, doi:10.1007/JHEP06(2010)043, arXiv:1002.2581.
- [17] J. Alwall et al., “The automated computation of tree-level and next-to-leading order differential cross sections, and their matching to parton shower simulations”, *JHEP* **07** (2014) 079, doi:10.1007/JHEP07(2014)079, arXiv:1405.0301.
- [18] M. L. Mangano, M. Moretti, F. Piccinini, and M. Treccani, “Matching matrix elements and shower evolution for Top-Quark Production in Hadronic Collisions”, *JHEP* **01** (2007) 013, doi:10.1088/1126-6708/2007/01/013, arXiv:hep-ph/0611129.
- [19] R. Field, “Min-bias and the underlying event at the LHC”, *Acta Physica Polonica B* **42** (20011) 2631, doi:10.5506/APhysPolB.42.2631, arXiv:1202.0901.
- [20] CMS Collaboration, “Electron reconstruction and identification at $\sqrt{s} = 7$ TeV”, CMS Physics Analysis Summary CMS-PAS-EGM-10-004, 2010.
- [21] CMS Collaboration, “Performance of muon identification in pp collisions at $\sqrt{s} = 7$ TeV”, CMS Physics Analysis Summary CMS-PAS-MUO-10-002, 2010.
- [22] CMS Collaboration, “Performance of CMS muon reconstruction in pp collision events at $\sqrt{s} = 7$ TeV”, *JINST* **7** (2012) P10002, doi:10.1088/1748-0221/7/10/P10002, arXiv:1206.4071.
- [23] CMS Collaboration, “Determination of Jet Energy Calibration and Transverse Momentum Resolution in CMS”, *JINST* **6** (2011) P11002, doi:10.1088/1748-0221/6/11/P11002, arXiv:1107.4277.
- [24] CMS Collaboration, “Commissioning of the Particle-Flow reconstruction in Minimum-Bias and Jet Events from pp Collisions at 7 TeV”, CMS Physics Analysis Summary CMS-PAS-PFT-10-002, 2010.
- [25] M. Cacciari, G. P. Salam, and G. Soyez, “The Anti-k(t) jet clustering algorithm”, *JHEP* **04** (2008) 063, doi:10.1088/1126-6708/2008/04/063, arXiv:0802.1189.
- [26] L. Sonnenschein, “Algebraic approach to solve $t\bar{t}$ dilepton equations”, *Phys. Rev. D* **72** (2005) 095020, doi:10.1103/PhysRevD.72.095020, arXiv:hep-ph/0510100.
- [27] L. Sonnenschein, “Analytical solution of $t\bar{t}$ dilepton equations”, *Phys. Rev. D* **73** (2006) 054015, doi:10.1103/PhysRevD.73.054015, arXiv:hep-ph/0603011. [Erratum: *Phys. Rev. D* **78**, 079902(2008), doi:10.1103/PhysRevD.78.079902].
- [28] “CT10 NLO and NNLO parton distribution functions”, (2014).
- [29] CMS Collaboration, “First Measurement of the Cross Section for Top-Quark Pair Production in Proton-Proton Collisions at $\sqrt{s} = 7$ TeV”, *Phys. Lett. B* **695** (2011) 424, doi:10.1016/j.physletb.2010.11.058, arXiv:1010.5994.
- [30] D. Bourilkov, R. C. Group, and M. R. Whalley, “LHAPDF: PDF use from the Tevatron to the LHC”, in *TeV4LHC Workshop - 4th meeting Batavia, Illinois, October 20-22, 2005*. 2006. arXiv:hep-ph/0605240.

-
- [31] M. Czakon, P. Fiedler, and A. Mitov, "Total Top-Quark Pair-Production Cross Section at Hadron Colliders Through $\mathcal{O}(\alpha_s^4)$ ", *Phys. Rev. Lett.* **110** (2013) 252004, doi:10.1103/PhysRevLett.110.252004, arXiv:1303.6254.
- [32] CMS Collaboration, "CMS Luminosity Based on Pixel Cluster Counting - Summer 2012 Update", CMS Physics Analysis Summary CMS PAS LUM-12-001, 2012.
- [33] G. Cowan, K. Cranmer, E. Gross, and O. Vitells, "Asymptotic formulae for likelihood-based tests of new physics", *Eur. Phys. J. C* **71** (2011) 1554, doi:10.1140/epjc/s10052-011-1554-0, arXiv:1007.1727. [Erratum: *Eur. Phys. J. C* **73**, 2501 (2013), doi:10.1140/epjc/s10052-013-2501-z].

A Appendix

Table 3: Selection efficiency times acceptance $\epsilon \cdot A$ in percentage and the statistical uncertainties for all 45 generated Littlest Higgs samples.

T' Mass [GeV]	W' Mass [GeV]	$\epsilon \cdot A$ [%]	T' Mass [GeV]	W' Mass [GeV]	$\epsilon \cdot A$ [%]
400	200	31.7 ± 0.2	1600	600	55.6 ± 0.2
600	200	38.8 ± 0.2	1600	800	54.8 ± 0.2
600	400	46.4 ± 0.2	1600	1000	53.7 ± 0.2
800	200	42.6 ± 0.2	1600	1200	51.7 ± 0.2
800	400	52.7 ± 0.2	1600	1400	46.9 ± 0.2
800	600	49.9 ± 0.2	1800	200	48.4 ± 0.2
1000	200	44.8 ± 0.2	1800	400	51.1 ± 0.2
1000	400	53.4 ± 0.2	1800	600	53.6 ± 0.2
1000	600	54.9 ± 0.2	1800	800	53.6 ± 0.2
1000	800	50.0 ± 0.2	1800	1000	53.1 ± 0.2
1200	200	47.4 ± 0.2	1800	1200	51.8 ± 0.2
1200	400	53.2 ± 0.2	1800	1400	49.7 ± 0.2
1200	600	55.7 ± 0.2	1800	1600	43.1 ± 0.2
1200	800	54.1 ± 0.2	2000	200	46.6 ± 0.2
1200	1000	48.3 ± 0.2	2000	400	50.0 ± 0.2
1400	200	48.2 ± 0.2	2000	600	51.4 ± 0.2
1400	400	52.8 ± 0.2	2000	800	50.8 ± 0.2
1400	600	55.6 ± 0.2	2000	1000	51.3 ± 0.2
1400	800	55.0 ± 0.2	2000	1200	49.6 ± 0.2
1400	1000	53.0 ± 0.2	2000	1400	47.1 ± 0.2
1400	1200	48.2 ± 0.2	2000	1600	45.7 ± 0.2
1600	200	49.0 ± 0.2	2000	1800	41.1 ± 0.2
1600	400	52.3 ± 0.2			

Table 4: Expected and observed upper limits for the Simplified Littlest Higgs results for all channels combined.

T' Mass [GeV]	W' Mass [GeV]	Observed	Expected		
			Median	68% C.L. Range	95% C.L. Range
400	200	0.0354	0.0487	[0.0350,0.0675]	[0.0265,0.0899]
600	200	0.0143	0.0182	[0.0131,0.0256]	[0.0099,0.0344]
600	400	0.0083	0.0114	[0.0082,0.0161]	[0.0061,0.0215]
800	200	0.0113	0.0081	[0.0058,0.0115]	[0.0043,0.0156]
800	400	0.0123	0.0067	[0.0048,0.0095]	[0.0036,0.0129]
800	600	0.0044	0.0057	[0.0040,0.0080]	[0.0030,0.0110]
1000	200	0.0031	0.0050	[0.0035,0.0071]	[0.0026,0.0097]
1000	400	0.0060	0.0050	[0.0036,0.0070]	[0.0027,0.0095]
1000	600	0.0054	0.0038	[0.0027,0.0055]	[0.0020,0.0076]
1000	800	0.0025	0.0040	[0.0028,0.0057]	[0.0021,0.0079]
1200	1000	0.0022	0.0028	[0.0020,0.0041]	[0.0014,0.0058]
1200	200	0.0017	0.0026	[0.0018,0.0039]	[0.0013,0.0056]
1200	400	0.0021	0.0032	[0.0022,0.0047]	[0.0017,0.0065]
1200	600	0.0027	0.0032	[0.0023,0.0046]	[0.0017,0.0064]
1200	800	0.0018	0.0026	[0.0018,0.0038]	[0.0013,0.0054]
1400	1000	0.0014	0.0021	[0.0014,0.0030]	[0.0010,0.0044]
1400	1200	0.0020	0.0019	[0.0013,0.0029]	[0.0009,0.0042]
1400	200	0.0011	0.0015	[0.0010,0.0023]	[0.0007,0.0035]
1400	400	0.0011	0.0018	[0.0012,0.0028]	[0.0009,0.0041]
1400	600	0.0013	0.0024	[0.0016,0.0034]	[0.0012,0.0048]
1400	800	0.0014	0.0023	[0.0016,0.0033]	[0.0012,0.0047]
1600	1000	0.0011	0.0019	[0.0013,0.0027]	[0.0009,0.0039]
1600	1200	0.0015	0.0016	[0.0011,0.0024]	[0.0008,0.0035]
1600	1400	0.0018	0.0015	[0.0010,0.0023]	[0.0007,0.0034]
1600	200	0.0008	0.0011	[0.0007,0.0017]	[0.0005,0.0026]
1600	400	0.0008	0.0012	[0.0008,0.0019]	[0.0005,0.0029]
1600	600	0.0008	0.0014	[0.0009,0.0021]	[0.0007,0.0032]
1600	800	0.0009	0.0017	[0.0011,0.0025]	[0.0008,0.0036]
1800	1000	0.0008	0.0013	[0.0009,0.0020]	[0.0006,0.0030]
1800	1200	0.0011	0.0015	[0.0010,0.0022]	[0.0007,0.0032]
1800	1400	0.0014	0.0013	[0.0009,0.0020]	[0.0006,0.0030]
1800	1600	0.0017	0.0013	[0.0008,0.0021]	[0.0006,0.0031]
1800	200	0.0007	0.0009	[0.0006,0.0014]	[0.0004,0.0022]
1800	400	0.0007	0.0010	[0.0006,0.0015]	[0.0004,0.0024]
1800	600	0.0007	0.0010	[0.0007,0.0016]	[0.0005,0.0025]
1800	800	0.0007	0.0012	[0.0008,0.0018]	[0.0005,0.0027]
2000	1000	0.0007	0.0010	[0.0006,0.0016]	[0.0004,0.0024]
2000	1200	0.0008	0.0011	[0.0007,0.0018]	[0.0005,0.0027]
2000	1400	0.0012	0.0013	[0.0009,0.0021]	[0.0006,0.0030]
2000	1600	0.0015	0.0013	[0.0008,0.0020]	[0.0006,0.0030]
2000	1800	0.0017	0.0012	[0.0008,0.0020]	[0.0006,0.0030]
2000	200	0.0007	0.0008	[0.0005,0.0014]	[0.0004,0.0021]
2000	400	0.0007	0.0008	[0.0005,0.0014]	[0.0004,0.0021]
2000	600	0.0007	0.0009	[0.0006,0.0014]	[0.0004,0.0022]
2000	800	0.0007	0.0010	[0.0006,0.0015]	[0.0004,0.0023]